

## Frequency non-degenerate sequential excitation of the impurity trapped exciton in strontium fluoride crystals doped with ytterbium

Pubudu S. Senanayake, Jon-Paul R. Wells, Michael F. Reid, Rosa B. Hughes-Currie, Giel Berden, Roger J. Reeves, and Andries Meijerink

Citation: *Journal of Applied Physics* **117**, 133109 (2015); doi: 10.1063/1.4916375

View online: <http://dx.doi.org/10.1063/1.4916375>

View Table of Contents: <http://scitation.aip.org/content/aip/journal/jap/117/13?ver=pdfcov>

Published by the AIP Publishing

### Articles you may be interested in

Intervalence charge transfer luminescence: Interplay between anomalous and 5d – 4f emissions in Yb-doped fluorite-type crystals

*J. Chem. Phys.* **141**, 234704 (2014); 10.1063/1.4902759

Yb 2+ -doped SrCl<sub>2</sub>: Electronic structure of impurity states and impurity-trapped excitons

*J. Chem. Phys.* **133**, 114509 (2010); 10.1063/1.3475562

Influence of trapping on the exciton dynamics of Al<sub>x</sub>Ga<sub>1-x</sub>As films

*Appl. Phys. Lett.* **86**, 111906 (2005); 10.1063/1.1885173


Photoluminescence of Yb<sup>3+</sup>-doped CuInS<sub>2</sub> crystals in magnetic fields

*J. Appl. Phys.* **89**, 2706 (2001); 10.1063/1.1341214

Crystal-field splitting of energy levels of rare-earth ions Dy<sup>3+</sup> (4f<sup>9</sup>) and Yb<sup>3+</sup> (4f<sup>13</sup>) in M(II) sites in the fluorapatite crystal Sr<sub>5</sub>(PO<sub>4</sub>)<sub>3</sub>F

*J. Appl. Phys.* **83**, 1009 (1998); 10.1063/1.366790

You don't  
still use this  
cell phone



or this computer



Why are you  
still using an  
AFM designed  
in the 80's?



**It is time to upgrade your AFM**

Minimum \$20,000 trade-in discount  
for purchases before August 31st

**Asylum Research is today's  
technology leader in AFM**

[dropmyoldAFM@oxinst.com](mailto:dropmyoldAFM@oxinst.com)



*The Business of Science®*

# Frequency non-degenerate sequential excitation of the impurity trapped exciton in strontium fluoride crystals doped with ytterbium

Pubudu S. Senanayake,<sup>1</sup> Jon-Paul R. Wells,<sup>2,a)</sup> Michael F. Reid,<sup>3</sup> Rosa B. Hughes-Currie,<sup>1</sup> Giel Berden,<sup>4</sup> Roger J. Reeves,<sup>1,3</sup> and Andries Meijerink<sup>5</sup>

<sup>1</sup>Department of Physics and Astronomy, University of Canterbury, PB 4800, Christchurch 8410, New Zealand

<sup>2</sup>The Dodd-Walls Centre for Photonic and Quantum Technologies and Department of Physics and Astronomy, University of Canterbury, PB 4800, Christchurch 8140, New Zealand

<sup>3</sup>MacDiarmid Institute for Advanced Materials and Nanotechnology and Department of Physics and Astronomy, University of Canterbury, PB 4800, Christchurch 8140, New Zealand

<sup>4</sup>Radboud University Nijmegen, Institute for Molecules and Materials, FELIX Facility, Toernooiveld 7, 6525 ED Nijmegen, The Netherlands

<sup>5</sup>Debye Institute for NanoMaterials Science, University of Utrecht, P.O. Box 80000, TA 3508 Utrecht, The Netherlands

(Received 21 December 2014; accepted 18 March 2015; published online 7 April 2015)

We model the dynamic behaviour observed for impurity-trapped excitons in  $\text{SrF}_2\text{:Yb}^{2+}$  using transient photoluminescence enhancement induced via a two-frequency, sequential excitation process employing an UV optical parametric amplifier synchronized to an IR free electron laser (FEL). We observe sharp transitions interpreted as a change of state of the localized hole and broad bands interpreted as a change of state of the delocalized electron. Our modeling indicates that the  $4f$  crystal-field interaction is 25% smaller than in  $\text{CaF}_2$ . The photoluminescence enhancement transients are analyzed across a range of excitation frequencies using a system of rate equations. The temporal behavior is explained in terms of intra-excitonic relaxation, local lattice heating by the FEL, and liberation of electrons from trap states. © 2015 AIP Publishing LLC. [<http://dx.doi.org/10.1063/1.4916375>]

## I. INTRODUCTION

Rare-earth doped crystals have found use in a wide variety of applications ranging from solid state laser systems to dosimeters for radiotherapy, due to their favorable optical and mechanical characteristics such as high quantum efficiency and durability.<sup>1</sup> The sharp optical transitions within the  $4f$  configuration of rare-earth ions allow detailed and accurate modeling of the energy levels.<sup>1,2</sup> However, the transitions involving excited configurations such as  $4f^{N-1}5d$  are more difficult to model, due to vibronic broadening of the spectra,<sup>3</sup> which provide less information than the sharp lines observed in intra- $4f$  spectra. Probing the excited configurations via a two-color sequential excitation experiment would yield more information about these configurations.<sup>3</sup>

*Ab-initio* calculations of excited-state electronic structure and bond lengths<sup>4,5</sup> confirm that sharp line transitions, as well as broad vibronic transitions, should be observable in excited state absorption. Experiments such as those proposed above would also allow for the testing and refinement of these models, as well as extension into structures with different symmetry.

Excited configurations can also involve charge transfer from the rare-earth to the next nearest cations in the crystal. These delocalized electrons form an exciton where the electron is loosely bound to the  $4f$  hole. Such excitons are termed impurity trapped excitons (ITEs). ITEs can act as mediators for non-radiative relaxation of the  $4f^{N-1}5d$  excited configuration and thereby form an important intermediate state in the optical de-excitation process.<sup>4,6</sup> In a few materials doped

with  $\text{Yb}^{2+}$  and  $\text{Eu}^{2+}$ , ITEs form the lowest energy emitting state,<sup>7</sup> giving rise to a strongly red-shifted and broad emission band (sometimes termed ‘anomalous emission’).<sup>8</sup> This substantial vibronic broadening arises because the electron-hole recombination gives a large bond length change.<sup>9</sup> Some information can be obtained from luminescence measurements, and low lying energy levels and dynamics have been inferred from indirect methods, such as the temperature dependence of photoluminescence and photoconductivity.<sup>9,10</sup> However, with a two-color excitation experiment, it is possible to probe the internal structure of ITEs directly.

Since ITEs are important intermediate states in the relaxation of the excited  $4f^{N-1}5d$  configuration, it is vital that more comprehensive knowledge of the energy level structure and dynamics is obtained. From previous studies of  $\text{SrF}_2\text{:Yb}^{2+}$  and  $\text{CaF}_2\text{:Yb}^{2+}$ ,<sup>9,11</sup> it is known that there are suitable meta-stable states for sequential excitation experiments, and due to the differing radiative relaxation rates of the lowest lying levels, it is possible to utilize a time domain, photoluminescence enhancement technique. Our previous work has illustrated this technique.<sup>12,13</sup> In this paper, we utilize the transient photoluminescence enhancement to experimentally determine the energy level structure of the ITE in  $\text{SrF}_2$  crystals doped with  $\text{Yb}^{2+}$ . The dynamics of the induced enhancement are described and modeled in detail.

## II. EXPERIMENTAL DETAILS

Strontium fluoride crystals doped with 0.05 mol. % ytterbium were grown in graphite crucibles using the vertical Bridgmann method in a 38 kW radio-frequency furnace at the University of Canterbury. The samples were grown in a

a)<sup>1</sup>jon-paul.wells@canterbury.ac.nz

vacuum of approximately  $10^{-3}$  Pa, at a lowering rate of  $4 \text{ mm h}^{-1}$ . Ytterbium was introduced to the charge as  $\text{YbF}_3$  with reduction occurring during the growth process. As a result, both the divalent and trivalent species are present in the crystal.

The transient photoluminescence enhancement technique utilizes pulsed excitation in the UV to populate the exciton ground state and a subsequent (delayed) IR pulse to probe the intra-excitonic transitions. A frequency doubled Quantronix TOPAS optical parametric amplifier (OPA) was used to provide 3 ps pulses at 360 nm with a repetition rate of 1 kHz. Output from the Dutch Free Electron Laser (FELIX) was used as the IR probe. The pulse structure of FELIX is comprised of 4–6  $\mu\text{s}$  macropulses having a repetition rate of 10 Hz. A given macropulse contains a train of micropulses separated by 40 ns, with a pulse length of several ps. In this experiment, a wavelength range from 6 to 90  $\mu\text{m}$  was used. Band pass filters were employed for IR wavelengths up to 20  $\mu\text{m}$  to block higher harmonics from FELIX. The OPA was synchronized to FELIX, and the timing between the UV and IR pulses could be electronically varied. The UV and IR beams were spatially overlapped at the sample, which was placed in an Oxford Instruments variable temperature cryostat. The peak UV fluence was  $14 \text{ mJ/cm}^2$ , and the IR energy density varied between 5 and  $11 \text{ J/cm}^2$ . The ITE emission was directed through a TRIAX 320 spectrometer and detected using a C31034 photomultiplier tube (PMT).

### III. RESULTS AND DISCUSSION

For excitation of the  $4f^{14} \rightarrow 4f^{13}5d$  absorption transitions of  $\text{Yb}^{2+}$  at 360 nm, emission between 650 and 850 nm, exhibiting a single exponential decay with a lifetime of 580  $\mu\text{s}$ , was detected from the sample (at 10 K), which is consistent with previous observations attributed to ITE emission.<sup>9</sup> As noted by Moine *et al.*,<sup>9</sup> the emission peaks in the near infra-red region of the spectrum and due to the wavelength dependent sensitivity of the PMT used in our experiments only the high energy side of the broad emission band could be detected.

#### A. Two-color excitation

Under two-color UV+IR excitation (with the IR pulse delayed by 100  $\mu\text{s}$  with respect to the UV pulse), a significant enhancement in the emission was observed, as shown in the inset of Fig. 1. The enhancement exhibits a bi-exponential decay and a rise time greater than the FELIX pulse length. The decay consists of a fast component which shows variation dependent upon the IR excitation frequency and a slow component with a decay constant of 580  $\mu\text{s}$ . The enhancement arises from the population of higher lying exciton states with larger radiative decay rates than the exciton ground state transition.<sup>12</sup>

Fig. 1 shows the behavior of the emission over a sequence of 100 UV pulses, which is one repetition cycle of the FEL. It is clear that there is a decrease in emission intensity envelope with each UV pulse. The IR pulse induces an increase in the emission, which then decreases over the subsequent UV pulses.

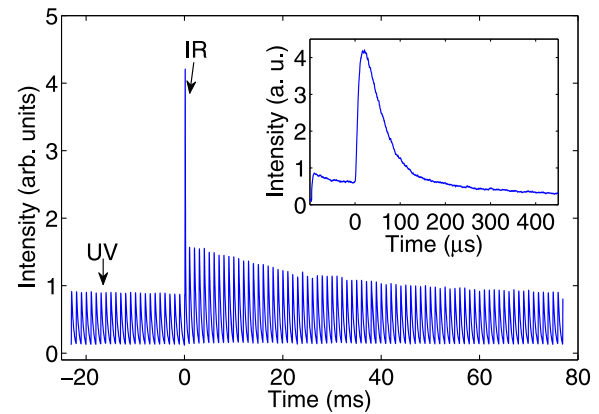


FIG. 1. Behavior of the transient signal over a 100 ms time scale. Each UV pulse populates trap states until a steady state is reached. These traps are then liberated by the IR pulse occurring at  $T=0$  ms. The IR frequency in this instance was  $550 \text{ cm}^{-1}$  (18  $\mu\text{m}$ ). The inset shows the enhancement observed under excitation by the IR pulse 100  $\mu\text{s}$  after the UV at the same excitation frequency but with a higher time resolution measurement. Emission was monitored at 695 nm.

This behavior can be explained if we assume that exciting the  $4f^{13}5d$  states not only creates ITE states but can also liberate electrons, which are then trapped. This would transform  $\text{Yb}^{2+}$  ions into  $\text{Yb}^{3+}$  giving fewer oscillators that can be excited by the UV photons. These trap states appear to be relatively long-lived, at least on the time scale presented in Fig. 1 (100 ms). The FEL pulse appears to reverse the process, liberating trapped electrons and increasing the number of  $\text{Yb}^{2+}$  sites. Since the UV induced emission tends to a steady state, either the available trap states are saturated, or a subset of the  $\text{Yb}^{2+}$  ions are remote from traps.

From the decay of the UV-excited peak heights, we can determine the fraction of electrons being trapped per pulse. The peak height may be fitted to an exponential function

$$I(n) = I_0 e^{-\beta n} + y_0, \quad (1)$$

where  $n$  is the pulse number following the IR pulse.

$I_0 = 0.80 \pm 0.04$  (arb. units) is the ratio of the intensity of the first peak *after* the IR pulse to the steady state peak intensity,  $y_0 = 0.82 \pm 0.03$  (arb. units), and  $\beta = 0.033 \pm 0.002$  (dimensionless).

Examining the ratio of  $y_0$  to  $I_0$ , we see that about *half* of the oscillators are lost to traps between each IR pulse, and these traps are then liberated by the IR pulse. The loss rate is approximately 3% per pulse, so the intensity reaches a steady-state value between each IR pulse. Assuming that the trap liberation is a single photon process, the traps are at most  $550 \text{ cm}^{-1}$  deep (the IR excitation frequency).

#### B. Infra-red excitation spectrum of $\text{SrF}_2:\text{Yb}^{2+}$

Variation of IR excitation frequency causes changes in both the intensity and dynamic behavior of the enhancement, particularly in the rise time and the fast decay components of the transient. Fig. 2 is an IR frequency–time plot which shows the observed changes in enhancement intensity and dynamic behavior between 550 and  $1300 \text{ cm}^{-1}$ . The sharp cutoff in enhancement intensity occurring around  $600 \text{ cm}^{-1}$

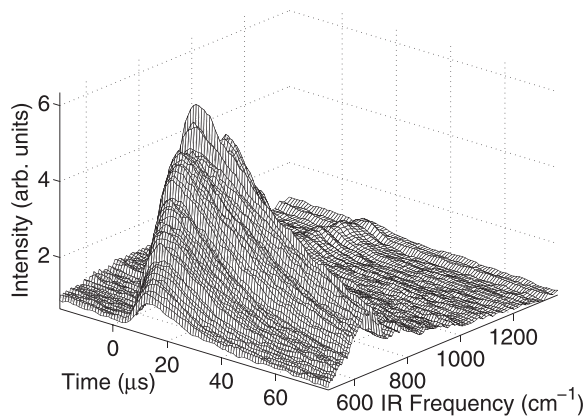


FIG. 2. Observed enhancement of photoluminescence  $\text{SrF}_2:\text{Yb}^{2+}$  under IR excitation after the initial UV excitation at 360 nm. The IR pulse occurs at 0  $\mu\text{s}$ ; the UV pulse was 100  $\mu\text{s}$  earlier. The emission was monitored with the grating of the spectrometer at zero order, i.e., the emission was integrated over all wavelengths.

is due to higher harmonic filters reducing the FEL fluence. A power correction is applied to the integrated spectra and individual transients, but not to the raw data presented in Fig. 2.

Integration of the time domain transient signal over the enhancement region yields an IR excitation spectrum of the ITE by scanning the FEL wavelength (Fig. 3(a)). The dips

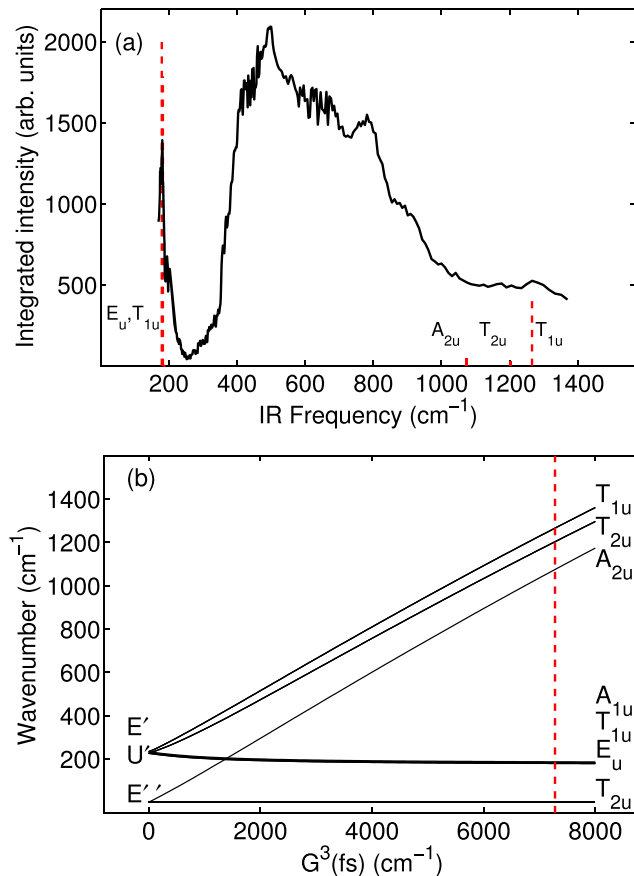


FIG. 3. (a) IR excitation spectrum for  $\text{SrF}_2:\text{Yb}^{2+}$  including the calculated oscillator strengths (shown as dashed lines) for the transitions observed. (b) Dependence of the exciton energy levels on the exchange parameter  $G^3$  (fs). The dashed vertical line corresponds to a value of 7278  $\text{cm}^{-1}$ , which results from a fit of the IR excitation spectrum.

within the broad band are due to atmospheric water absorption. The spectrum can be divided into three distinct regions, with a peak centered at  $(1284 \pm 8) \text{ cm}^{-1}$  having a FWHM of  $(40 \pm 10) \text{ cm}^{-1}$ , a broad band from 950 to 400  $\text{cm}^{-1}$ , and a low energy peak at  $(178 \pm 3) \text{ cm}^{-1}$  with a FWHM of  $(12 \pm 2) \text{ cm}^{-1}$ . The modeling described below suggests that the lower part of the broad band is due to localized heating by IR absorption by the lattice and the higher-energy part (950 to 700  $\text{cm}^{-1}$ ) is due to intra-excitonic transitions. This behavior is similar to previous observations in  $\text{CaF}_2:\text{Yb}^{2+}$ .<sup>12</sup>

We interpret the broad band as a transition for which the state of the delocalized electron (where the electron is delocalized over the next nearest neighbor cations, while still being bound to the  $\text{Yb}^{3+}$ ) changes. This would affect the bonding between the  $\text{Yb}^{3+}$  and the nearest anions and lead to vibronic broadening. However, the broadening observed here (at most 300  $\text{cm}^{-1}$ ) is much smaller in comparison to that of exciton emission, where peak widths are typically on the order of 3000  $\text{cm}^{-1}$ .<sup>8,9,11,14</sup> Therefore, we infer that the bond length change is smaller than in the emission to  $4f^{14}$ .

We also attribute the sharp lines to intra-excitonic transitions. Since they are sharp, they cannot involve a change in bonding, thus they must be a result of excitations in the localized  $4f^{13}$  core (or “hole state”). Following Ref. 12, we use the following Hamiltonian for a  $4f^{13}$  configuration coupled to an  $s$  electron in a cubic crystal field:

$$H_{\text{cf}} = \zeta A_{\text{so}} + B^4 \left( C_0^4 + \sqrt{\frac{5}{14}} [C_4^4 + C_{-4}^4] \right) + B^6 \left( C_0^6 - \sqrt{\frac{7}{2}} [C_4^6 + C_{-4}^6] \right) + G^3(\text{fs}) g_3(\text{fs}). \quad (2)$$

Here,  $\zeta$  is the spin-orbit interaction for the 4f electrons,  $B^4$  and  $B^6$  are crystal-field parameters for the 4f electrons, and  $G^3(\text{fs})$  is the exchange interaction between the 4f and the delocalized electron. With this, we may model the energies and relative intensities of the sharp lines.

Since only two sharp lines were observed, not all the parameters in the model could be determined using the data. Consequently,  $\zeta$  and the ratio  $\frac{B^6}{B^4}$  were set to literature values (Table I). With these values and using  $B^4 = -600 \text{ cm}^{-1}$  and  $G^3(\text{fs}) = 7278 \text{ cm}^{-1}$ , the observed sharp lines could be reproduced by solving the Hamiltonian presented earlier, giving the line positions shown in Fig. 3.

The crystal field parameter  $B^4$  is lower than the corresponding value of  $-800 \text{ cm}^{-1}$  for  $\text{CaF}_2$ . Given the larger size of the  $\text{SrF}_2$  lattice,<sup>16,17</sup> this is reasonable and matches

TABLE I. Comparison of parameters used to fit the sharp lines observed in  $\text{SrF}_2:\text{Yb}^{2+}$  and  $\text{CaF}_2:\text{Yb}^{2+}$ . The  $\zeta$  and  $\frac{B^6}{B^4}$  values are from Lesniak.<sup>15</sup> All values are in wavenumbers ( $\text{cm}^{-1}$ ).

Parameter	$\text{SrF}_2:\text{Yb}^{2+}$	$\text{CaF}_2:\text{Yb}^{2+}$
$\zeta$	2928	2928
$B^4$	-600	-800
$\frac{B^6}{B^4}$	-0.34	-0.34
$G^3(\text{fs})$	7278	5900



favorably with previous studies on SrF<sub>2</sub> containing erbium and dysprosium impurities.<sup>15,18</sup> It is also comparable to the SrCl<sub>2</sub>:Yb<sup>2+</sup> value of  $-725 \text{ cm}^{-1}$ .<sup>19</sup>

The manner in which the exchange parameter affects the excitonic energy levels is demonstrated in Fig. 3(b). A simple model of the exciton<sup>8</sup> has the electron delocalized over the next nearest Sr<sup>2+</sup> ions. However, the comparatively large exchange parameter here indicates that the electron spends less time over the metal cations than in the CaF<sub>2</sub> case. Due to the larger lattice size in SrF<sub>2</sub>, this behavior seems reasonable. A summary of the fit parameters is presented in Table I, with the CaF<sub>2</sub> values included for comparison. Note that the  $B^4$  parameter for Yb<sup>3+</sup> in cubic sites in CaF<sub>2</sub> is considerably larger,  $-1710 \text{ cm}^{-1}$ .<sup>20</sup> This suggests that the bond length in the excited state is still considerably larger than for a Yb<sup>3+</sup> ion.

As shown in Fig. 3(b), when the  $G^3(fs)$  parameter is set to zero, the  $^2F_{7/2}$  multiplet of  $4f^{13}$  is split into  $E''$ ,  $U'$ , and  $E'$  irreducible representations of the octahedral group by the cubic crystal-field.<sup>21</sup> As  $G^3(fs)$  is increased, these states couple with  $^2S$  (from the delocalized  $s$ -like electron). For cubic symmetry, only magnetic dipole transitions will be allowed. The calculated intensities are compared with experiment in Fig. 3(a), which illustrates that several transitions are forbidden or calculated to be very weak.

Though the excited electron will be more delocalized than a  $6s$  electron in atomic Yb<sup>2+</sup>, the delocalization of the outer part of the wavefunction has little effect on the  $G^3(fs)$  parameter, since only that part of the wavefunction which is close to the  $4f$  hole is significant to the coupling between the  $f$  and  $s$  states.

### C. Exciton dynamics

The temporal transients are modeled with a system of rate equations for radiative and non-radiative transitions between the various exciton levels and the ground state ( $4f^{14}$ ). The analysis is similar to our analysis for NaMgF<sub>3</sub>:Yb<sup>2+</sup> in Ref. 13. While for NaMgF<sub>3</sub>:Yb<sup>2+</sup> trap liberation by the IR pulse was found to be crucial to modeling the transients, it is different for SrF<sub>2</sub>:Yb<sup>2+</sup> where trap liberations only play a role for the sharp low-energy transitions (Sec. III A), so we omit it in our initial description. However, since the transitions we examine here are at much longer wavelengths than those examined in NaMgF<sub>3</sub>:Yb<sup>2+</sup>, we find that heating of the lattice by the IR radiation plays a crucial role.

The energy levels shown in Fig. 4 are:

- (1) the ground state of Yb<sup>2+</sup>;
- (2) the ground state of the impurity trapped exciton, with radiative rate  $A_{21}$ ;
- (3) the lowest excited state of the impurity trapped exciton, separated by an energy of  $\epsilon = 26 \text{ cm}^{-1}$  from the ground state, with radiative rate  $A_{31}$ ;
- (4) the higher-energy exciton states.

Previous studies have established that the ITE has two emitting states,<sup>9,11</sup> separated by an energy of  $\epsilon = 26 \text{ cm}^{-1}$ . The meta-stable ground state has a slow radiative rate of  $A_{21} = 40 \text{ s}^{-1}$  and the upper excited state has a much faster radiative rate of  $A_{31} = 49000 \text{ s}^{-1}$ . The lowest lying meta-stable state (2) has a total decay rate of  $1720 \text{ s}^{-1}$  due to non radiative

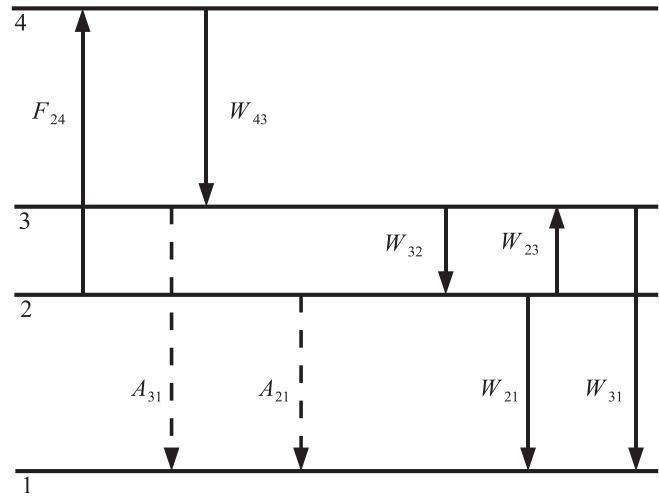


FIG. 4. Schematic diagram of the states and transitions used in the rate equation model. State 1 is the  $4f^{14}$  ground state. State 2 is the lowest meta-stable level, and state 3 is the first excited level of the exciton. State 4 is an ITE state situated above states 2 and 3.  $A_{ij}$  denote radiative transition rates, while  $W_{ijk}$  denote non-radiative transition rates.  $F_{24}$  represents the intra-exciton, IR induced transition rate.

relaxation to the ground state. Therefore, if the first excited state (3) is populated using IR excitation, an increase in emission intensity will occur. In our experiment, excitation of state 3 occurs via the absorption of IR photons from state 2 which then populate state 3 via a higher energy state 4. Non-radiative decay from state 4 to 3 likely occurs on a picosecond time-scale.  $W_{32}$ , the non radiative relaxation rate from state 3 to 2 was determined in this work.  $F_{24}$ , the intra-exciton IR induced transition rate varies with IR wavelength and fluence (Table II provides a summary of the parameters in this section).

The set of coupled rate equations corresponding to Fig. 4 are:

$$\begin{aligned}
 \frac{dN_1}{dt} &= A_{21}N_2 + A_{31}N_3 + W_{21}N_2 + W_{31}N_3, \\
 \frac{dN_2}{dt} &= -A_{21}N_2 - W_{21}N_2 - F_{24}f(t)N_2 \\
 &\quad - W_{23}(T)N_2 + W_{32}N_3, \\
 \frac{dN_3}{dt} &= -A_{31}N_3 - W_{31}N_3 - W_{32}N_3 \\
 &\quad + W_{23}(T)N_2 + W_{43}N_4, \\
 \frac{dN_4}{dt} &= -W_{43}N_4 + F_{24}f(t)N_2.
 \end{aligned} \tag{3}$$

In these equations,  $N_k$  is the population of a given state  $k$ . The function  $f(t)$  is the time dependent pulse shape of the IR excitation, which is recorded during the experiment.  $W_{23}$  is related to  $W_{32}$  via below equation

$$W_{23} = \frac{g_3}{g_2} W_{32} e^{-\epsilon/k_B T}, \tag{4}$$

where  $\epsilon = 26 \text{ cm}^{-1}$  and  $T$  is the temperature in Kelvin. The degeneracies associated with the respective levels,  $g_2 = 1$  and  $g_3 = 3$ , are adopted from Ref. 11. In Ref. 11, the rates  $W_{21}$  and  $W_{31}$  depend on temperature. However, they may be taken as constant in the temperature range considered here.

TABLE II. Parameters used in modeling of transients. The  $A_{ij}$  parameters are from previous work on  $\text{SrF}_2:\text{Yb}^{2+}$  ITE.<sup>11</sup> The non radiative parameters  $W_{21}$  and  $W_{31}$  have been calculated from the parameters of Ref. 11 for a temperature of 8.0 K.

Parameter	Value ( $\text{s}^{-1}$ )	Source
$A_{21}$	40	Reference 11
$A_{31}$	49000	Reference 11
$W_{21}$	1720	Reference 11
$W_{31}$	0.94	Reference 11
$W_{32}$	40 000	This work
$W_{43}$	infinite	This work
$F_{24}$	variable	This work

## D. Local heating

The local change in temperature due to absorption of the IR pulse determines  $W_{23}$  via Eq. (4). We calculate the time-evolution of the temperature from the measured IR fluence and literature values of IR absorption and heat capacity for  $\text{SrF}_2$ . IR absorption is highly dependent on IR wavelength, and heating becomes significant below about  $800\text{ cm}^{-1}$ . However, below  $400\text{ cm}^{-1}$ , IR absorption becomes so strong that the fluence at the region of the sample where the IR and UV beams intersect reduces, and hence, the effect of heating reduces.

We employ the following piecewise function to account for the temperature change under IR excitation:

$$\frac{dT}{dt} = \begin{cases} 0 & \text{pre IR} \\ E_m \frac{G(x,t)}{C(T)} & \text{during IR} \\ \alpha(T) \nabla^2 T & \text{post IR.} \end{cases} \quad (5)$$

$T$  is dependent upon  $(x, t)$ ,  $E_m$  is the maximum energy imparted by the IR pulse on the system, and is dependent upon the output fluence of the FEL and the IR absorption at a given frequency by the  $\text{SrF}_2$  lattice.  $G(x, t)$  is a Gaussian function describing the spatial distribution of the IR beam that changes in time according to  $f(t)$ , the temporal FEL pulse shape. We take advantage of cylindrical symmetry along the beam path. The time and position dependent energy is converted to a temperature with the use of  $C(T)$ , the heat capacity of pure  $\text{SrF}_2$ , which is a temperature dependent quantity. At low temperatures, the heat capacity increases rapidly, by two orders of magnitude from 2 to 40 K.<sup>22</sup> From the end of the IR pulse, the temperature of the local incident area decreases as the heat dissipates due to the induced temperature gradient.

This cooling effect is modeled by solving the heat equation in one dimension (taking advantage of the symmetry of the system). This is computed numerically, as the presence of  $\alpha(T) \propto \frac{k(T)}{C(T)}$ , the thermal diffusion coefficient which also has a strong temperature dependence, complicates the possible solutions. Here,  $k(T)$  is the temperature dependent thermal conductivity of  $\text{SrF}_2$ , obtained from previous studies.<sup>23,24</sup> Prior to the IR pulse, we assume that the local environment is at the lattice temperature. Using the instantaneous temperature of the system computed from Eq. (5) in

Eq. (4), a time dependent non radiative rate from state 2 to 3 is derived. This gives a time dependent population profile of the states, which is combined with the Einstein  $A_{ij}$  coefficients to give a time dependent emission profile.

The macropulse is measured to carry up to 8 mJ per pulse. Using the known absorption properties<sup>25,26</sup> of  $\text{SrF}_2$  combined with its specific heat capacity<sup>22</sup> and considering heat transfer, we compute that at  $500\text{ cm}^{-1}$ , the temperature at the focus of the IR beam rises by up to 10 K. One should keep in mind that this temperature change is local to the IR beam spot and is not the temperature of the entire sample (in contrast to Moine *et al.*). The heating contributes to the rise time observed in the IR induced enhancement, as it initiates a thermally activated population change from state 2 to 3 (see Eq. (4)). As the IR fluence increases, more energy is deposited in the sample, which takes longer to dissipate, leading to increasing rise times (see Sec. III F). Furthermore, the delay between the UV and IR pulses has little impact on the amount of energy released into the system as heat, thus a change in the delay would not cause a change in the rise, nor a change in the overall shape of the enhancement in the time domain.

## E. Determination of parameters

In Ref. 9,  $W_{32}$  was treated as effectively infinite because, in those experiments, the populations of levels 2 and 3 were in thermal equilibrium. In our experiments, the IR pulse leaves the system in a non-equilibrium state, and the value of  $W_{32}$  is required for the modeling described above. We fix  $W_{32}$  by fitting an exponential decay curve of the form

$$I(t) = I_0[e^{-A_{31}t} + e^{-W_{21}t} + e^{-W_{32}t}] + y_0 \quad (6)$$

at an IR excitation frequency of  $910\text{ cm}^{-1}$ . At  $910\text{ cm}^{-1}$ , the IR pulse does not cause much heating of the sample, and therefore, the decay of the transient is predominantly due to the three pathways represented in the equation ( $A_{21}$  and  $W_{31}$  give negligible contributions.).

By employing Beer's law, the relative IR fluence at the surface (facing the incoming IR beam) of the volume where the two lasers are interacting is found. Integrating the IR fluence across the volume gives the total energy deposited. Because the IR absorption is heavily frequency dependent, this gives a deposited energy "spectrum" across the IR excitation frequencies, with peak heating occurring at  $500\text{ cm}^{-1}$  (see Sec. III J).

$E_m$  (see Eq. (5)) is found by employing the modeling described in Sec. III D.  $E_m$  is left as a free parameter when modeling the transient that is most influenced by the local heating (i.e., transient due to IR excitation at  $500\text{ cm}^{-1}$ ). The  $E_m$  values for other excitation frequencies are calculated by scaling the maximum value by the heating spectrum.

For any particular IR excitation frequency,  $F_{24}$  is determined through least squares fitting. Therefore, it serves as an indication of the relative cross-section of the direct excitation of intra-excitonic states by the IR. Both  $F_{24}$  and  $E_m$  are scaled according to incident IR fluence when conducting fluence measurements at a particular excitation frequency.

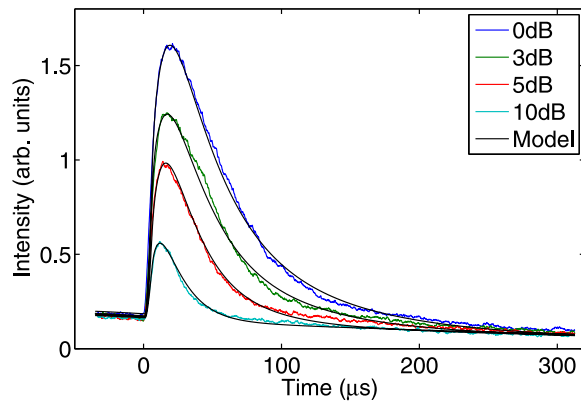


FIG. 5. Fluence dependent photoluminescence enhancement for IR excitation at  $500\text{ cm}^{-1}$ . Modeled curves, as described by Eqs. (3) and (5), are also included to show the goodness of fit. 0dB indicates a fluence of  $10\text{ J cm}^{-2}$ , which is attenuated as indicated by the decibel level.

### F. IR fluence dependent dynamic behavior

Increasing the IR fluence increases the magnitude of the enhancement as shown in Fig. 5. Saturation is seen while doubling the IR fluence from  $5.0$  to  $10\text{ J cm}^{-2}$ , with the intensity of the enhancement increasing by less than a factor of two. The change of fluence also causes a change in the shape of the transients, with the rise time of the enhancement increasing with fluence. Additionally, the photoluminescence enhancement decay rate also increases. Such fluence dependent behavior is also observed across other excitation frequencies.

Table III summarizes the values of the intra-excitonic parameters from the model and the maximum temperature reached for a given fluence for excitation at  $500\text{ cm}^{-1}$ . Fig. 5 shows the modeled transients with the corresponding experimental transients. The system is likely to have a frequency dependent interaction cross section for transitions within the ITE and has a frequency dependent lattice absorption profile. Leaving  $F_{24}$  free and by changing the total energy input to reflect the change in IR absorption with frequency (see Sec. III E) the model was also able to successfully compute the transients for an IR excitation at  $770\text{ cm}^{-1}$ . The details of the computations are presented in Table IV.

The differences between  $F_{24}$  at the two excitation frequencies indicate that although the transients are significantly different, both in shape and enhancement magnitude (Fig. 6), the intra-excitonic component of the enhancement is actually larger at  $770\text{ cm}^{-1}$  excitation than at  $500\text{ cm}^{-1}$ . While the overall enhancement is largest for  $500\text{ cm}^{-1}$

TABLE III. Parameters from modeling the fluence dependent transients at an IR excitation frequency of  $500\text{ cm}^{-1}$ .  $T_{\text{max}}$  indicates the maximum temperature reached by the sample with the excitation volume.

Fluence ( $\text{J cm}^{-2}$ )	$F_{24}$ ( $\text{s}^{-1}$ )	$E_m$ (mJ)	$T_{\text{max}}$ (K)
$10.0 \pm 0.1$	$12500 \pm 300$	$4.30 \pm 0.10$	$18.2 \pm 0.2$
5.0	$6250 \pm 130$	$2.15 \pm 0.05$	15.8
3.1	$4160 \pm 80$	$1.33 \pm 0.04$	14.5
1.0	$1250 \pm 30$	$0.43 \pm 0.01$	$12.4 \pm 0.1$

TABLE IV. Parameters from modeling the fluence dependent transients at an IR excitation frequency of  $770\text{ cm}^{-1}$ . With due consideration of the absorption effects of the IR pulse,  $E_m$  was calculated to be  $0.85\text{ mJ}$  at maximum fluence and was subsequently scaled for the varying fluences employed.

Fluence ( $\text{J cm}^{-2}$ )	$F_{24}$ ( $\text{s}^{-1}$ )	$E_m$ (mJ)	$T_{\text{max}}$ (K)
$10.0 \pm 0.1$	$16100 \pm 600$	$0.85 \pm 0.03$	$13.5 \pm 0.3$
5.0	$8100 \pm 300$	$0.43 \pm 0.02$	12.4
3.1	$5200 \pm 100$	$0.27 \pm 0.01$	11.3

excitation, the  $F_{24}$  parameter indicates that the absorption cross section of the exciton is higher at  $770\text{ cm}^{-1}$ . Thus, the majority of the enhancement at  $500\text{ cm}^{-1}$  is due to local heating. This implies that the direct intra-excitonic transition peak would be at a higher energy than can be directly observed from the excitation spectrum in Fig. 3(a).

The modeling confirms that as the fluence increases, the maximum temperature reached  $T_{\text{max}}$  increases sublinearly, explaining the observed saturation effect in the transients (see Fig. 5). Incorporating the temperature dependent nature of the diffusion coefficient into the model also accounts for the varying shape of the enhancement at a given IR fluence. As the heat capacity of the sample increases sharply with temperature<sup>22</sup> while the thermal conductivity increases less rapidly,<sup>23</sup> these observations are unsurprising.

By extracting the time evolution of the relative populations of states 1, 2, and 3 from the model, it can be seen that only a small proportion of the population gets excited from state 2 to 3, and this is reflected in the magnitude of the  $F_{24}$  parameter. Fig. 7 shows the complete population change under the influence of the IR. We see that excitation into state 3 is very small with  $<10\%$  of the population occupying state 3 at a given time. This indicates that the absorption cross section is weak.

Fig. 8(a) shows the changes of population in state 3 for IR excitation at  $500\text{ cm}^{-1}$ , which confirms that the majority of the population transfer, and hence the enhancement, is due to heating. Fig. 8(b) shows the population changes for IR excitation at  $770\text{ cm}^{-1}$ . It is clear that the direct intra-excitonic absorption plays a much larger relative role at this frequency.

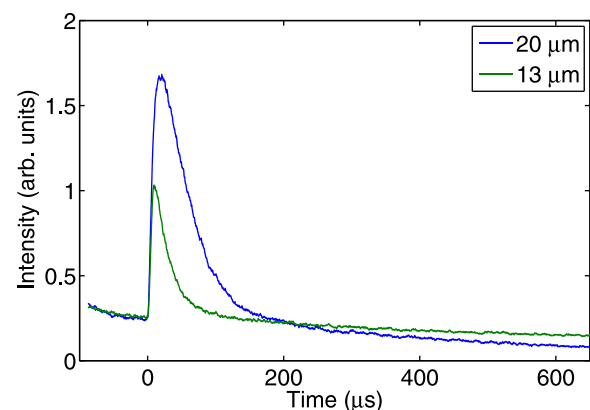


FIG. 6. Comparison between the full fluence transients at IR frequencies of  $500\text{ cm}^{-1}$  ( $20\text{ }\mu\text{m}$ ) and  $770\text{ cm}^{-1}$  ( $13\text{ }\mu\text{m}$ ) for a sample temperature of  $10\text{ K}$ .

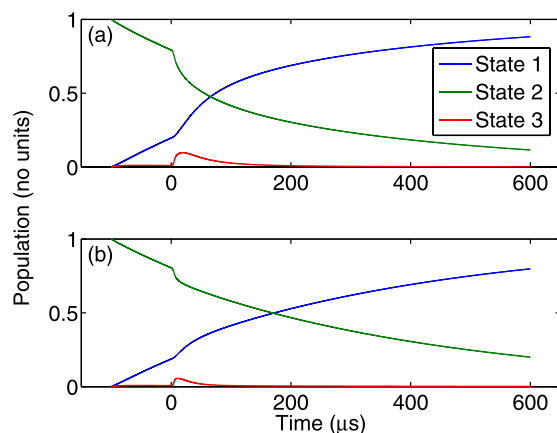


FIG. 7. Change in the relative populations of states 1, 2, and 3 under IR excitation. The total population is 1, and the initial conditions place all the population in state 2. The ambient lattice temperature causes thermalization and sets up a population distribution that is time dependent. (a) shows the changes for IR excitation at  $500\text{ cm}^{-1}$  and (b)  $770\text{ cm}^{-1}$ . Note the difference in the relative populations of state 3 in (a) and (b).

### G. Effect of UV–IR delay on dynamic behavior

Increasing the delay between the UV and IR pulses causes the photoluminescence enhancement to decrease in amplitude (Fig. 9). The intensity of the enhancement is proportional to the emission level just prior to the incidence of the IR pulse, and as the UV–IR delay is increased, the emission level decreases (due to the decay of oscillators from state 2 to 1). This decrease implies that at least a component of the enhancement is directly dependent on the number of excitons occupying in state 2, and that the enhancement is caused by a temporal rearrangement of the emitting exciton ensemble.

The shape of the photoluminescence enhancement transients does not change as the UV–IR delay is varied. This behavior is observed at all IR excitation frequencies studied (Fig. 10). The delay dependent decrease in the amplitude of the enhancement is exponential with a decay time of approximately  $470\text{ }\mu\text{s}$  at all wavelengths measured. This is similar to the decay time of the emission under UV only excitation at approximately  $500\text{ }\mu\text{s}$ .

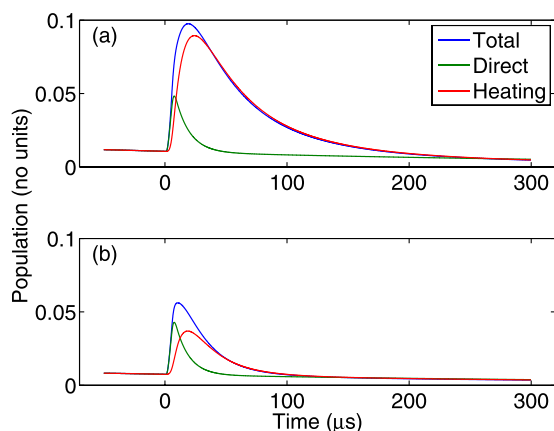


FIG. 8. Population of state 3 due to heating and direct intra-excitonic absorption for (a) IR excitation at  $500\text{ cm}^{-1}$  and (b)  $770\text{ cm}^{-1}$ .

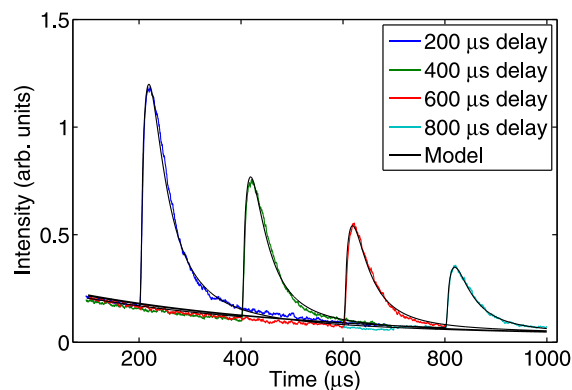


FIG. 9. Photoluminescence enhancement as a function of varying delay between the UV and IR pulses. The black trace indicates the modeled fit to the data and shows excellent agreement. IR excitation was at  $500\text{ cm}^{-1}$ .

Fig. 11 shows the dependence of the enhancement magnitude on the level of the emission prior to the IR pulse. The relationship is linear and repeatable across different IR excitation frequencies. Although the gradients vary, the relationship remains linear which indicates that infrared excitation is not adding to the emitting population.

Our modeling confirms that the enhancement is predominantly determined by the number of oscillators in state 2 rather than the addition of liberated traps (see Fig. 9), since the temporal dynamics are unchanged as the UV–IR delay is varied.

### H. Effect of sample temperature on dynamic behavior

As the sample temperature is increased, photoluminescence enhancement steadily decreases, as shown in Fig. 12. This is because when the populations in states 2 and 3 thermalize, there is a less population in state 2 available for redistribution by IR excitation. The rate equation model was able to accommodate the temperature dependent behavior with a fixed change in ambient temperature,  $T_a$ .

In the fitting process both  $F_{24}$  and  $E_m$ , the energy absorbed as heat, remained constant at the value used when computing the full fluence transient at an excitation frequency

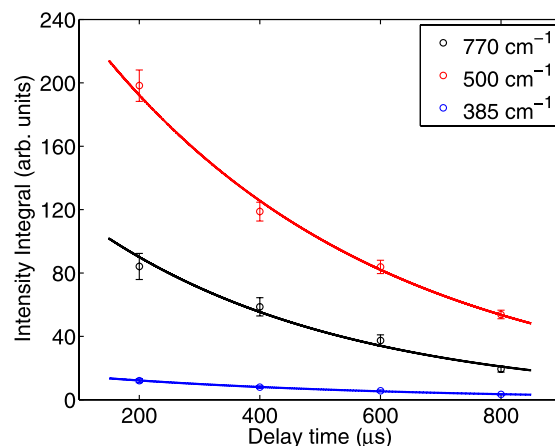


FIG. 10. Change in the IR induced enhancement magnitude with varying UV–IR delay at different IR excitation frequencies. The solid lines are exponential decay fits to the delay dependent enhancement. The enhancement magnitude is determined by integrating over the enhancement period and subtracting the UV only contribution.



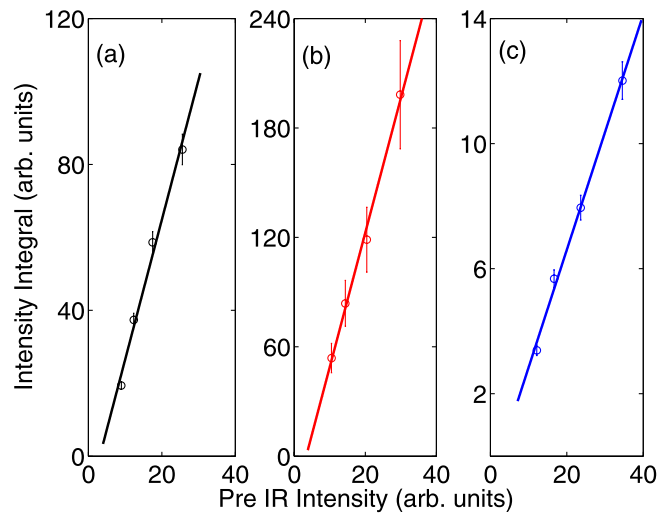


FIG. 11. Change in the IR induced enhancement magnitude with pre-IR emission level at different excitation frequencies (a)  $770\text{ cm}^{-1}$ , (b)  $500\text{ cm}^{-1}$ , and (c)  $385\text{ cm}^{-1}$ . The enhancement magnitude has a linear dependence upon the pre-IR emission level.

of  $770\text{ cm}^{-1}$ . The parameters are given in Table V. The invariance observed in the modeling is expected as the decrease in the enhancement due to intra-excitonic absorption is driven by the population of state 2 being greatly reduced at  $t=0$  as the temperature increases. We also note that as the sample temperature increases,  $T_{\text{max}} - T_a$  decreases. This is consistent with the previous fits and the known dependence of heat capacity upon temperature.<sup>22</sup>

From the temperature dependent transients, it is clear that thermalization is a significant process in determining the dynamic properties of this system, even at low temperatures due to the small energy gap of  $26\text{ cm}^{-1}$  between states 2 and 3.

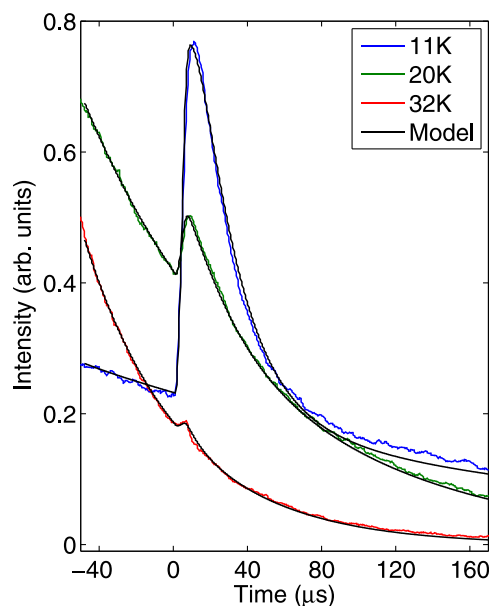


FIG. 12. Temperature dependent photoluminescence enhancement for IR excitation at  $770\text{ cm}^{-1}$ . The data are time matched at the IR pulse incidence, represented by  $t=0\text{ }\mu\text{s}$ . The UV pulse occurred at  $-100\text{ }\mu\text{s}$ . The modeled fit is shown in black.

TABLE V. Optimized parameters from modeling the temperature dependent transients at an IR excitation frequency of  $770\text{ cm}^{-1}$  shown in Fig. 12. The sample temperature ( $T_a$ ) was varied in the model to reflect the indicated temperature of the cryostat;  $T_{\text{max}}$  is the maximum temperature the interaction volume reaches under the IR pulse.  $\Delta T$  shows the increase in temperature from the overall sample temperature.

$T_a$ (K)	$T_{\text{max}}$ (K)	$\Delta T$ (K)	$F_{24} (\pm 700) (\text{s}^{-1})$
11.0	14.2	3.2	16 700
20.0	20.7	0.7	16 600
32.5	32.7	0.2	16 700

### I. Transient photoluminescence enhancement of the $178\text{ cm}^{-1} T_{2u} \rightarrow E_u$ transition

The rate equation model may be applied to the sharp intra-exciton transition at  $178\text{ cm}^{-1}$ , yielding a good fit to the measured enhancement. In this case, the  $F_{24}$  parameter was inferred to be  $12900 \pm 600\text{ s}^{-1}$ , and  $E_m$  was found to be  $0.4\text{ mJ}$  giving  $T_{\text{max}} = 12\text{ K}$ . However, as Fig. 13(a) shows, there is a long time offset that is not well modeled with the above parameters. Unlike the dynamics modeled in Sections III F and III G, the slope of the long term transient does not cause it to converge to the pre-IR emission level in time. Since an offset remains when heating is taken into account, the long term emission is not caused by heating of the sample alone.

Fig. 13(b) shows the fit achieved by allowing IR liberated traps to populate state 2 at a rate of  $10^5\text{ s}^{-1}$  from the onset of the IR pulse for its duration. The pulse shape  $f(t)$  is again used to account for the changing IR intensity across the IR pulse. The  $F_{24}$  and  $E_m$  values were unchanged between the two fits. The offset present in the transient can be reproduced by the introduction of liberated traps into state 2.

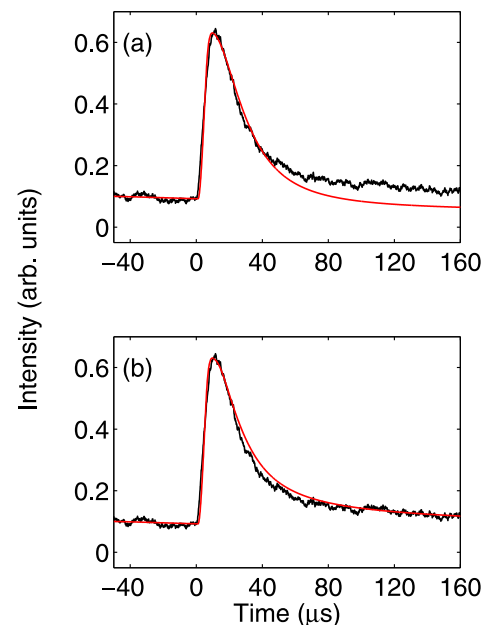


FIG. 13. Transient photoluminescence enhancement for IR excitation at  $178\text{ cm}^{-1}$ . The solid line is the model fit with  $F_{24} = 12900 \pm 600\text{ s}^{-1}$  and  $E_m = 0.4\text{ mJ}$ . (a) shows the fit achieved with heating alone, and (b) shows the fit achieved when, in addition to the heating, the effect of trap liberation was included.

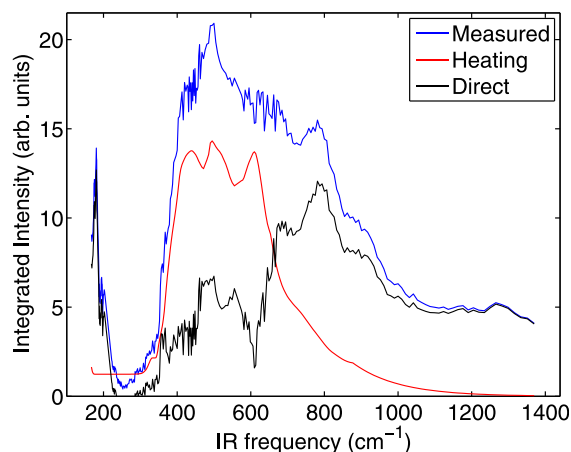


FIG. 14. IR excitation spectrum for  $\text{SrF}_2:\text{Yb}^{2+}$  including the effect of heating. The “heating” curve is a simulated curve based on the calculated energy input into the system by the FEL. The “direct” curve is extracted by taking the difference between the measurement and the simulated heating curve. We infer that it represents the IR excitation spectrum of the direct transitions within the ITE.

The analysis in Sec. III A shows that the liberation of traps does occur at higher excitation frequencies. However, from the dynamic analysis Sections III F–III H, it appears not contribute to the emission. It is possible that the configurational change in the ITE is different under excitation at  $178\text{ cm}^{-1}$  compared to the higher frequencies. This difference may allow liberated electrons to relax into the excited states of the ITE, producing the observed enhancement. Comparison of  $F_{24}$  for excitation at  $178\text{ cm}^{-1}$  and  $770\text{ cm}^{-1}$  shows that the transition moments are comparable.

### J. Deconvolution of exciton spectrum from heating

We have described above how the effect of local heating may be calculated. If we integrate the results of that calculation, we can estimate the contribution of heating to the spectrum of Fig. 3. The results are shown in Fig. 14. Without further investigation, it is unclear if the resulting multiple peaks between  $400$  to  $1000\text{ cm}^{-1}$  are true representations of ITE states. However, the calculation shows that the most intense feature within the broad region is at a higher energy than the measured spectrum suggests. Additionally, the heating model provides an explanation for the sharp intensity decrease in the excitation spectrum at the  $400\text{ cm}^{-1}$  mark.

## IV. CONCLUSION

We have performed a comprehensive study of the energy levels and dynamics of impurity trapped excitons in  $\text{SrF}_2:\text{Yb}^{2+}$  using a transient photoluminescence enhancement technique. The measured energy levels and the relative intensities of the observed transitions can be accounted for in terms of the exchange interaction between a  $4f$  hole and an  $s$  electron within a cubic crystal field. The temporal behavior of the measured photoluminescence enhancement is

interpreted via a rate equation model incorporating intra-excitonic excitation and relaxation as well as some local lattice heating. There is also evidence of the liberation of traps but to a lesser degree than in other materials studied such as  $\text{MgF}_2:\text{Yb}^{2+}$  (Ref. 27) and  $\text{NaMgF}_3:\text{Yb}^{2+}$ .<sup>13</sup> It is possible that this reflects the fact that clustering of trivalent ytterbium ions (also present in the material) is less significant in the  $\text{SrF}_2$  host when compared with  $\text{MgF}_2$  and  $\text{NaMgF}_3$ .

## ACKNOWLEDGMENTS

This work was supported by the Marsden fund of the Royal Society of New Zealand via Grant No. 09-UOC-080. The authors acknowledge the support of the Dutch FOM (Stichting voor Fundamenteel Onderzoek der Materie) organization in providing the required beamtime on FELIX. We would like to thank the FELIX staff for their assistance. P.S.S. and R.H.-C. acknowledge the support of the University of Canterbury via PhD studentships.

- <sup>1</sup>B. Jacquier and G. K. Liu, *Spectroscopic Properties of Rare Earths in Optical Materials*, Springer Series in Materials Science (Springer, 2005).
- <sup>2</sup>W. T. Camall, G. L. Goodman, K. Rajnak, and R. S. Rana, *J. Chem. Phys.* **90**, 3443 (1989).
- <sup>3</sup>M. F. Reid, L. Hu, S. Frank, C. K. Duan, S. Xia, and M. Yin, *Eur. J. Inorg. Chem.* **2010**, 2649.
- <sup>4</sup>G. Sánchez-Sanz, L. Seijo, and Z. Barandiarán, *J. Chem. Phys.* **133**, 114509 (2010).
- <sup>5</sup>G. Sánchez-Sanz, L. Seijo, and Z. Barandiarán, *J. Chem. Phys.* **133**, 114506 (2010).
- <sup>6</sup>M. Grinberg and S. Mahlik, *J. Non-Cryst. Sol.* **354**, 4163 (2008).
- <sup>7</sup>D. S. McClure and C. Pedrini, *Phys. Rev. B* **32**, 8465 (1985).
- <sup>8</sup>P. Dorenbos, *J. Phys.: Condens. Matter* **15**, 2645 (2003).
- <sup>9</sup>B. Moine, B. Courtois, and C. Pedrini, *J. Phys.* **50**, 2105 (1989).
- <sup>10</sup>C. Pedrini, M. F. Joubert, and D. McClure, *J. Lumin.* **125**, 230 (2007).
- <sup>11</sup>B. Moine, B. Courtois, and C. Pedrini, *J. Lumin.* **48**, 501 (1991).
- <sup>12</sup>M. F. Reid, P. S. Senanayake, J. P. R. Wells, G. Berden, A. Meijerink, A. J. Salkeld, C. K. Duan, and R. J. Reeves, *Phys. Rev. B* **84**, 113110 (2011).
- <sup>13</sup>R. B. Hughes-Currie, P. S. Senanayake, J.-P. R. Wells, M. F. Reid, G. Berden, R. J. Reeves, and A. Meijerink, *Phys. Rev. B* **88**, 104304 (2013).
- <sup>14</sup>S. Lizzo, A. Meijerink, G. J. Dirksen, and G. Blasse, *J. Phys. Chem. Solids* **56**, 959 (1995).
- <sup>15</sup>K. Lesniak, *J. Phys. Condens. Matter* **2**, 5563 (1990).
- <sup>16</sup>R. E. Thoma, *Inorg. Chem.* **1**, 220 (1962).
- <sup>17</sup>A. Kiel and W. B. Mims, *Phys. Rev. B* **6**, 34 (1972).
- <sup>18</sup>D. J. Newman and B. Ng, *Crystal Field Handbook* (Cambridge University Press, 2000).
- <sup>19</sup>Z. Pan, C. K. Duan, and P. A. Tanner, *Phys. Rev. B* **77**, 085114 (2008).
- <sup>20</sup>V. Petit, P. Camy, J.-L. Doualan, X. Portier, and R. Moncorge, *Phys. Rev. B* **78**, 085131 (2008).
- <sup>21</sup>B. Henderson and G. F. Imbusch, *Optical Spectroscopy of Inorganic Solids* (Clarendon Press, Oxford, 1989).
- <sup>22</sup>S. J. Collocott and J. G. Collins, *J. Phys. C. Solid State Phys.* **16**, 6179 (1983).
- <sup>23</sup>J. A. Harrington and C. T. Walker, *Phys. Rev. B* **1**, 882 (1970).
- <sup>24</sup>R. O. Pohl, X. Liu, and E. Thompson, *Rev. Mod. Phys.* **74**, 991 (2002).
- <sup>25</sup>W. Kaiser, W. G. Spitzer, R. H. Kaiser, and L. E. Howarth, *Phys. Rev.* **127**, 1950 (1962).
- <sup>26</sup>P. Denham, G. R. Field, P. L. R. Morse, and G. R. Wilkinson, *Proc. R. Soc. A* **317**, 55 (1970).
- <sup>27</sup>P. S. Senanayake, J. P. R. Wells, M. F. Reid, G. Berden, A. Meijerink, and R. J. Reeves, *Appl. Phys. Lett.* **100**, 041902 (2012).